Journal of Materials Chemistry C

ROYAL SOCIETY OF CHEMISTRY

PAPER

View Article Online
View Journal | View Issue

Cite this: J. Mater. Chem. C, 2025, 13, 23269

Structures and optical properties of cyclic-ether complexes of europium/ytterbium made *via* a redox approach

Lara-Pauline Faden, [a] Carsten Donsbach,[a] Radian Popescu, [b] Lkhamsuren Bayarjargal, [c] Yolita M. Eggeler, [b] Björn Winkler [c] and Claus Feldmann *[a]

To obtain cyclic-ether complexes of europium/ytterbium with generally less preferable cyclic ethers (*i.e.*, those with large/small ring openings, cage-type cryptands, and N-containing crown ethers), a novel redox approach is used. Accordingly, 24-crown-8 (24c8), benzo-15-crown-5 (benzo-15c5), *N*-phenylaza-15-crown-5 (pac), [2.2.2]cryptand (c222), and kryptofix21 (k21) are made to react with europium and ytterbium metal nanoparticles, 2–4 nm in size. Europium and ytterbium are selected as both lanthanides are flexible in their oxidation state (II/III), and cover a typical range of cation radii ($r(Eu^{2+})$: 139 pm to $r(Yb^{3+})$: 113 pm) in the 4f-row (radii for CN = 8). As a result, $[Yb(24c8)]_4[AlCl_4]_8$·THF (**1**), $[Eu(benzo\text{-}15c5)_2]I_2$ (**2**), $[Yb(benzo\text{-}15c5)_2]I_2$ (**3**), $[BMIm][Eu_4Cl_4(pac)_4][AlCl_4]_5$ (**4**), $[\{Yb(pac)\}_2(\mu\text{-}Cl)_2][AlCl_4]_2$ (**5**), $[EuCl(c222)][AlCl_4]$ (**6**), [EuI(c222)]I (**7**), $[\{Yb(c222)\}_2(\mu\text{-}Cl)]_2[AlCl_4]_6$·1.5THF (**8**), $[BMIm]\text{-}[Yb(c222)]I_3$ (**9**), $[Eu(k21)_2]I_2$·naph (**10**), and $[BMIm][\{Yb(k21)\}_2(\mu\text{-}Cl)_3]I_2$ (**11**) are obtained as new compounds. The title compounds show various coordination scenarios with mono- to tetranuclear building units. All are luminescent with a narrow-line blue emission of **4** and the strong second harmonic generation (SHG) effect of **6** being specifically interesting. As the redox approach used here leads to the coordination of the lanthanide cations with all applied cyclic ethers – although exhibiting less preferred size and/or coordinative binding with the lanthanide cation – it may present a novel synthesis strategy to generally prepare new metal complexes with cyclic ethers with interesting optical, magnetic or catalytic properties.

Received 22nd July 2025,
Accepted 13th October 2025

DOI: 10.1039/d5tc02776d

rsc.li/materials-c

1. Introduction

Cyclic ethers, such as crown ethers or cryptands, are widely applied as versatile ligands for the coordination of metal cations.[1] Due to the specific ligand diameter and the strong chelating properties, metal cations can be coordinated with high selectivity, which allows qualitative as well as quantitative determination and even selective separation.[2] Within the manifold of metals, coordination of lanthanide cations with cyclic ethers was less often described.[3] Among such lanthanide-based complexes, 18-crown-6 (18c6) or its derivatives were reported most often as ligands,[1,4] which can be ascribed to the typical size range of $Ln^{2+/3+}$ cations (100–130 pm),[5] that fits well with the ring-opening diameter of 18c6 (about 300 pm).[6] Generally, crown-ether coordination of Ln^{2+}/Ln^{3+} allows realization of stable complexes with rigid bonding, often resulting in interesting optical/luminescent,[7] magnetic[8] or catalytic properties.[9]

While complexes of the lanthanides were reported most often with 18c6 (about 120 crystal structures),[10] significantly fewer reports have addressed complexes with the smaller 15c5 (about 30 crystal structures),[10] or the larger 24c8 (about 5 crystal structures).[10] This holds similarly for the coordination of lanthanides with cryptands (especially in the case of the larger Ln^{2+} cations).[11] Coordination with aza-crown ethers is even less preferred in comparison to crown ethers and cryptands due to the predominantly oxophilic character of the lanthanides.[12] Moreover, the synthesis of complexes with lanthanides coordinated by cyclic ethers is usually performed *via* Lewis-acid–base reactions or salt metathesis reactions.[3,7–9,11,12] As such reactions are usually performed in coordinating solvents and/or in the presence of further ligands, the lanthanides are often coordinated by further ligands in

[a] Institute for Inorganic Chemistry, Karlsruhe Institute of Technology (KIT), Engesserstrasse 15, D-76131 Karlsruhe, Germany. E-mail: claus.feldmann@kit.edu
[b] Laboratory for Electron Microscopy, Karlsruhe Institute of Technology (KIT), Engesserstraße 7, D-76131 Karlsruhe, Germany
[c] Institute of Geosciences, Goethe University Frankfurt, Altenhoeferallee 1, D-60438 Frankfurt a. M., Germany

addition to the cyclic ether, whereas sole coordination of lanthanide cations by cyclic ethers and halide ligands is rare.

Aiming at the coordination of lanthanide cations with generally less preferred cyclic ethers, we here examine a redox approach using nanosized lanthanide metals as starting materials. As exemplary lanthanide metals, we have selected europium and ytterbium as both are flexible with regard to their oxidation state (II/III) and cover the typical size range of the 4f-element cation radii with europium as the largest ($r(Eu^{2+})$: 139 pm)[5] and ytterbium as the smallest ($r(Yb^{3+})$: 113 pm)[5] cation (all radii for coordination number 8). As cyclic ethers, the large 24-crown-8 (24c8), the small benzo-15-crown-5 (benzo-15c5) as well as the N-containing ethers *N*-phenylaza-15-crown-5 (pac), the cage-like [2.2.2]cryptand (c222) and the N–H-acidic kryptofix 21 (k21) have been selected. After the synthesis of the Eu(0) and Yb(0) nanoparticles, 2–4 nm in size, the redox approach resulted in 11 new compounds, including all applied cyclic ethers, showing various coordination scenarios, and interesting structural and optical properties with luminescence and second harmonic generation (SHG).

2. Experimental

Details regarding the synthesis of Eu(0) and Yb(0) nanoparticles, the synthesis of title compounds **1–11**, and the analytical methods are provided in the SI.

3. Results and discussion

3.1 Europium and ytterbium metal nanoparticles

To examine reactions of lanthanide-metal nanoparticles with cyclic ethers, we have selected europium and ytterbium. Divalent europium represents the largest cation ($r(Eu^{2+})$: 139 pm)[5] while trivalent ytterbium is one of the smallest cations ($r(Yb^{3+})$: 113 pm)[5] in the 4f row (all radii for coordination number 8). Thus, both can be considered as representatives for the whole group of 4f metals in terms of radii and the di/trivalent oxidation state. The synthesis of Eu(0) and Yb(0) nanoparticles generally follows our previously reported approach to prepare reactive base-metal nanoparticles in the liquid phase.[13] Thus, EuI_2 and $YbCl_3$ were used as the most common starting materials. In the case of europium, EuI_2 was dissolved in THF. Afterwards, a solution of lithium naphthalenide ([LiNaph]) in THF was injected into the EuI_2 solution with vigorous stirring. The formation of Eu(0) nanoparticles is indicated by the instantaneous formation of a deep-black suspension (Fig. 1). The synthesis of Yb(0) nanoparticles follows the synthesis of Eu(0) nanoparticles, in principle. Due to the insufficient solubility of $YbCl_3$, however, lithium, naphthalene, and $YbCl_3$ were simultaneously added to THF. After 12 hours of intense stirring, the reduction and nucleation of the Yb(0) nanoparticles were completed and also resulted in a deep-black suspension (Fig. 1). At first sight, the latter synthesis conditions seem disadvantageous for the nucleation of small-sized nanoparticles. However, several aspects support controlled nucleation also in the case of Yb(0). First of all, the dissolution of $YbCl_3$ is very slow whereas the reduction due to the instantaneously formed [LiNaph] is very fast. Moreover, the zerovalent metal is highly insoluble in THF.[13] Both support rapid nucleation and, thus, the formation of small-sized Yb(0) nanoparticles. For purification, the as-prepared Eu(0) and Yb(0) nanoparticles were centrifuged/redispersed in/from THF to remove remaining naphthalene and LiCl. Finally, the Yb(0) and Eu(0) metal nanoparticles were redispersed in THF to obtain colloidally stable suspensions. Alternatively, they can be dried at room temperature in a vacuum to obtain powder samples with a yield of about 80–90%. Losses mainly occur due to incomplete centrifugation of the nanoparticles. While we reported on Eu(0) nanoparticles before,[13a] liquid-phase synthesis of Yb(0) nanoparticles is shown here for the first time. Yb(0) nanoparticles are yet generally only accessible *via* physical methods (*i.e.* laser ablation).[14] Moreover, synthesis of Yb(0) nanoparticles in water was suggested,[15] which, however, is hardly credible with regard to the position of zerovalent ytterbium in the voltage series (E^0(bulk ytterbium: −2.2 V)[16] and also in conflict with the reactivity that we observed for our metal nanoparticles.

Particle size and particle size distribution of the as-prepared Eu(0) and Yb(0) nanoparticles were examined by transmission electron microscopy (TEM). TEM images show spherical particles with a uniform size and a low degree of agglomeration (Fig. 2). A statistical evaluation of >100 nanoparticles on TEM images reveals mean sizes of 2–4 nm (Table 1). High-resolution (HR)TEM images confirm the size of the nanoparticles and evidence the monocrystallinity of the as-prepared Eu(0) and Yb(0) nanoparticles with lattice fringes extending through the whole particle (Fig. 2). The lattice plane distances are well in agreement with the respective bulk metals (Table 1). This finding is also confirmed by Fourier-transform (FT) analysis, which is in accordance with the calculated diffraction pattern of hexagonal bulk europium ($P6_3/mmc$, a = 3.398, c = 5.385 Å) in the [101] zone axis,[17] and cubic bulk ytterbium ($Fm\bar{3}m$, a = 5.485 Å) in the [101] zone axis.[18] The intensity of the Bragg reflections is low due to the low scattering power of the small-sized metal nanoparticles in combination with their high mass and absorption coefficient.

The surface conditioning of the Eu(0) and Yb(0) nanoparticles was examined by Fourier-transform infrared (FT-IR) spectroscopy and by elemental analysis (C/H/N analysis) (see the SI). FT-IR spectra predominantly show weak vibrations of naphthalene as well as very weak vibrations related to THF (SI: Fig. S1). Exemplary C/H/N analysis of the Yb(0) nanoparticles confirms these results with a C/H content of 34.1/2.8 wt% (see the SI). The resulting C : H ratio of 12.2 is close to the ratio expected for a surface adsorption of naphthalene (C : H = 14.9). This finding is different from transition-metal nanoparticles that show a predominant surface functionalization with THF.[13] Total organic combustion analysis with thermogravimetry (TG) of the Yb(0) nanoparticles shows a solid residue of 71.4 wt%, which was identified as Yb_2O_3 *via* X-ray powder diffraction (SI: Fig. S2). This relates to a metal content of 63 wt% Yb for the as-

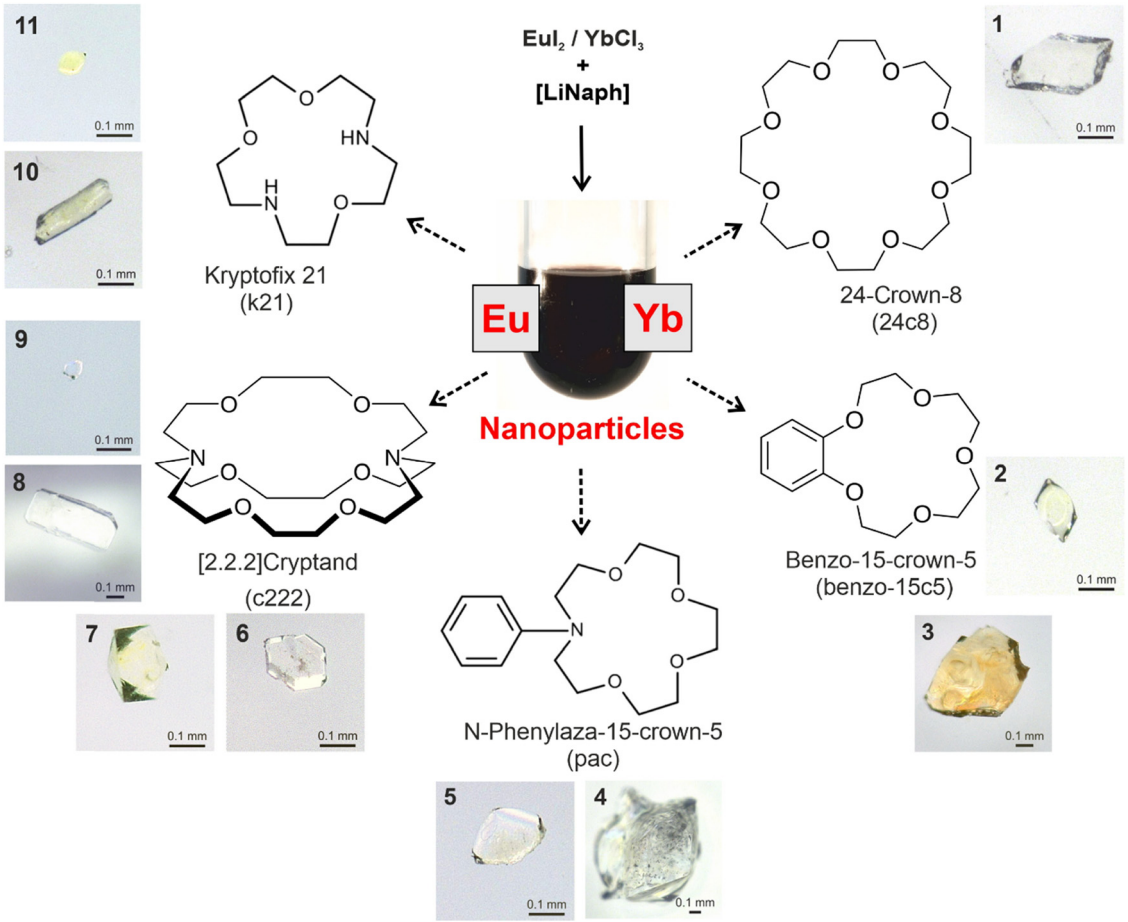

Fig. 1 Scheme illustrating the synthesis of Eu(0) and Yb(0) nanoparticles (exemplary suspension of Yb(0) nanoparticles shown), followed by the reaction of the as-prepared Eu(0) and Yb(0) nanoparticles with the cyclic ethers 24c8, benzo-15c5, pac, c222, and k21 with photos of single crystals of the obtained complexes **1–11**.

prepared nanoparticles. The related organic content is to be expected with regard to the particle size of the as-prepared metal nanoparticles and a monomolecular layer of naphthalene.

Due to the small particle size and the absence of strongly-binding and/or high-molecular-weight stabilizers on the particle surface, high reactivity of the as-prepared Eu(0) and Yb(0) nanoparticles is to be expected. Indeed, they show violent reactions when in contact with moisture, air, or other oxidizing agents, which lead to immediate combustion and/or explosion.[13] In fact, the reactivity of the Eu(0) and Yb(0) nanoparticles is comparable to the heavy alkali metals rubidium and cesium. Therefore, all reactions and sample handling need to be performed with inert conditions (argon, nitrogen, and vacuum), using standard Schlenk techniques or glove boxes. This also includes all centrifugation and analytical characterization.

3.2 Cyclic-ether complexes

For the reaction with the Eu(0) and Yb(0) nanoparticles, the large 24-crown-8 (24c8), the small benzo-15-crown-5 (benzo-15c5), as well as the N-containing cyclic ethers *N*-phenylaza-15-crown-5 (pac), the cage-like [2.2.2]cryptand (c222) and the N–H-acidic kryptofix 21 (k21) have been selected as cyclic ethers (SI: Table S1). Since the coordination of di- and trivalent rare-earth-metal cations by standard crown ethers such as 15-crown-5 and 18-crown-6 is straightforward using ionic-liquid-based syntheses,[7d] we here specifically focus on more complicated, less preferable cyclic ligands.

Syntheses were performed in the ionic liquids [BMIm]Cl/$AlCl_3$ or [BMIm]I as solvents (BMIm: butyl-3-methylimidazolium). Since [BMIm]Cl has a melting point of 70 °C, $AlCl_3$ was added to form [BMIm][$AlCl_4$], which is already liquid at room temperature. These ionic liquids feature good thermal stability, weakly coordinating properties, and good solubility of EuI_2 and $YbCl_3$.[19] In contrast to conventional polar solvents (*e.g.*, ethanol, THF, and DMF), the weakly coordinating properties of the ionic liquid allow avoiding coordination of the lanthanide cation by the solvent. After oxidation of the Eu(0)/Yb(0) nanoparticles, only the halides (Cl^-, $[AlCl_4]^-$, I^-) are available as anions, which supports the coordination of $Eu^{2+/3+}$/$Yb^{2+/3+}$ with the respective cyclic ether. A certain disadvantage of the ionic liquid relates to the difficult separation of the product and ionic liquid subsequent to synthesis because the solubility of the product and the ionic liquid is very similar.

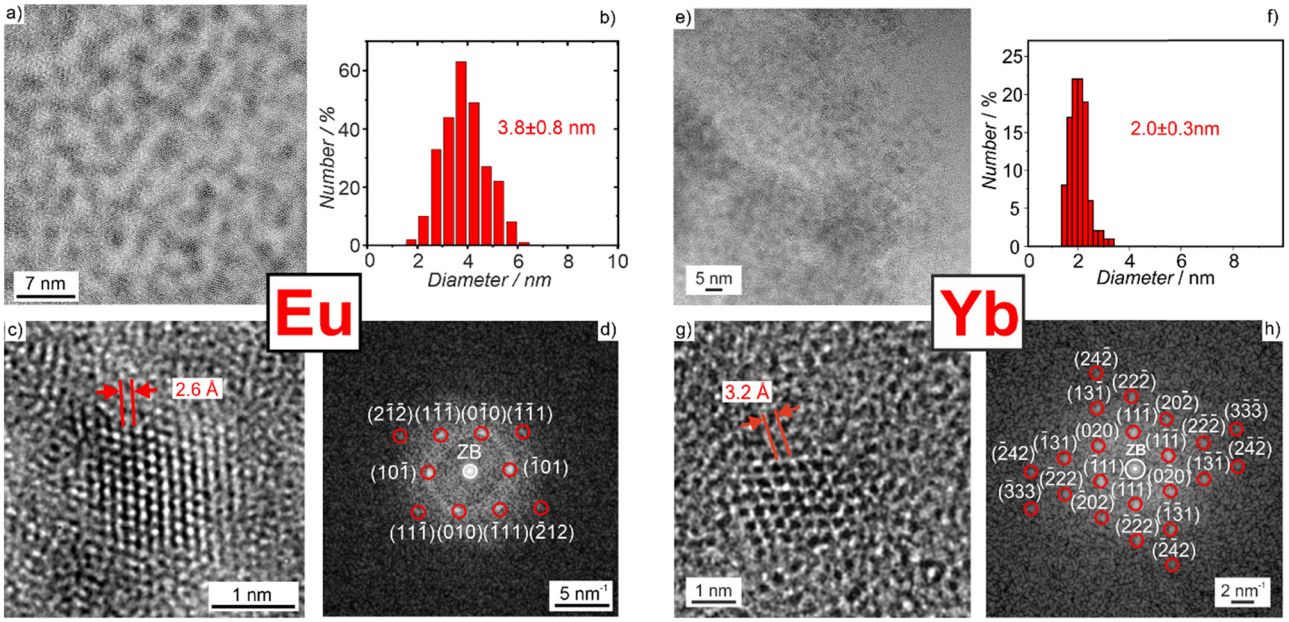

Fig. 2 Size and size distribution of the Eu(0) and Yb(0) nanoparticles: (a) and (e) TEM overview image, (b) and (f) size distribution based on a statistical evaluation of >200 nanoparticles on TEM images, (c) and (g) HRTEM image of a single Eu(0)/Yb(0) nanoparticle with lattice fringes, (d) and (h) FT pattern of the single nanoparticle shown in (c) and (g). Red circles indicate the diffraction pattern of hexagonal bulk europium in the [101] zone axis (d) and of cubic bulk ytterbium in the [101] zone axis (h) (zero-order beam (ZB) marked by a white circle).

Table 1 Mean size and lattice plane distances of Eu(0) and Yb(0) nanoparticles

Metal	Mean size/nm	Measured lattice plane distance/Å	Lattice plane distance of bulk reference/Å
Eu(0)	3.8 ± 0.8	2.6	2.6 (d_{101} of hexagonal europium)[17]
Yb(0)	2.0 ± 0.3	3.2	3.2 ($d_{\bar{1}11}$ of cubic ytterbium)[18]

To address this concern, we used small portions of cooled CH_2Cl_2 (0 °C) to wash the crystals of the title compounds and to remove most of the ionic liquid. An adsorption of the remaining ionic liquid on the crystal surfaces, however, can hardly be avoided.

With regard to the oxidation of the Eu(0) and Yb(0) nanoparticles, there are three options. First of all, Al^{3+} can be reduced to Al(0) if [BMIm]Cl/$AlCl_3$ is used as an ionic liquid.[20] Moreover, the $[BMIm]^+$ cation can be reduced, which is well-known in the literature, for instance, to obtain N-heterocyclic carbenes (NHCs),[21] or to trigger the reductive absorption and storage of carbon dioxide in imidazolium-type ionic liquids.[22] Finally, N–H acidic cyclic ethers such as k21 can release H_2 and, thereafter, become available as $[k21]^-$ or $[k21]^{2-}$ anions.[12] In principle, we have already observed all these options for the oxidation of the base-metal nanoparticles.[23] Due to the high reactivity of the Eu(0)/Yb(0) nanoparticles, all reactions could be performed at room temperature and resulted in, altogether, 11 new complexes (SI: Table S2). While the redox reactions are fast, in principle (*i.e.* some days at room temperature), the growth of sufficient single crystals takes a certain time (*i.e.* 4–8 weeks at room temperature). Most importantly, coordination was successful with all applied cyclic ethers and resulted in a wide range of coordination scenarios (Fig. 3–5).

As a very first example, 24c8 was reacted with Eu(0) and Yb(0) nanoparticles in [BMIm]Cl/$AlCl_3$ at room temperature. While no crystalline compound was obtained with europium, in the case of ytterbium colorless crystals of $[Yb(24c8)]_4[AlCl_4]_8 \cdot THF$ (**1**) were obtained with the reduction of Al^{3+} of the ionic liquid (SI: Table S2 and Fig. S3):

$$12\ Yb(0) + 12\ 24c8 + 32\ AlCl_3 + 3THF \rightarrow 3\ [Yb(24c8)]_4[AlCl_4]_8 \cdot THF + 8\ Al$$

The formation of aluminium is indicated by a greyish precipitate, slowly occurring during the reaction.

Surprisingly, **1** shows a coordination of Yb^{2+} by all eight oxygen atoms of 24c8 (Table 2 and Fig. 3a). Formation and crystallization of such a compound are difficult due to the

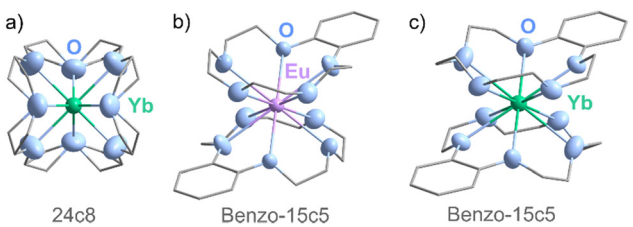

Fig. 3 Structure of (a) $[Yb(24c8)]^{2+}$ cation in **1**, (b) $[Eu(benzo\text{-}15c5)_2]^{2+}$ cation in **2**, (c) $[Yb(benzo\text{-}15c5)_2]^{2+}$ cation in **3** (unit cells displayed in SI: Fig. S3–S5).

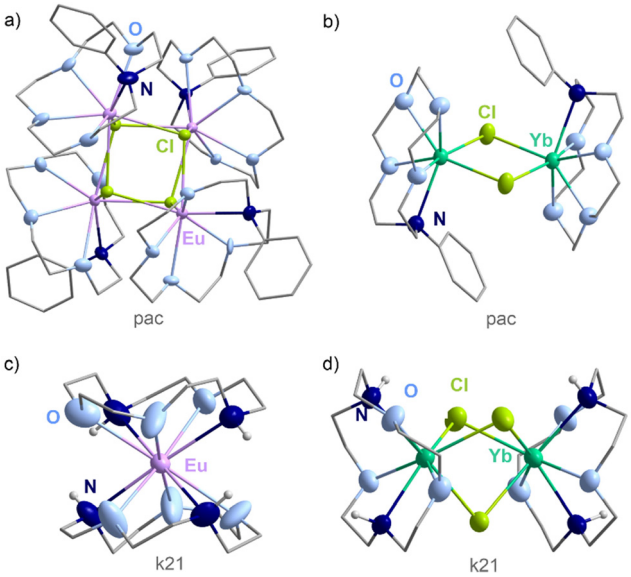

Fig. 4 Structure of (a) $[Eu_4Cl_4(pac)_4]^{4+}$ cation in **4**, (b) $[\{Yb(pac)\}_2(\mu\text{-}Cl)_2]^{2+}$ cation in **5**, (c) $[Eu(k21)_2]^{2+}$ cation in **10**, (d) $[\{Yb(k21)\}_2(\mu\text{-}Cl)_3]^{+}$ cation in **11** (unit cells displayed in SI: Fig. S6, S7, S12 and S13).

flexibility of the 24c8 molecule that can rotate around all 24 tetrahedral (C) and pseudo-tetrahedral (O) centers. Only recently, we could realize [Eu(III)Cl(24c8)]I_2 as the very first example with κ_8-coordination of 24c8 and a lanthanide cation.[24] The Yb–O distances are very similar (246.2(10)–247.6(13) pm) and show high parameters of thermal motion due to the positional disorder of 24c8 (see the SI). $[AlCl_4]^-$ originating from the ionic liquid serves as the anion. Furthermore, a THF molecule, originating from the synthesis of the Yb(0) nanoparticles, is present in the unit cell but, surprisingly, remains non-coordinated (SI: Fig. S3 and S14a). Obviously, a coordination of Yb^{2+} by 24c8 is preferred over Eu^{2+}, which is in agreement with the size of Yb^{2+} (128 pm, CN = 8)[5] and the ring opening of 24c8 (450–500 nm).[6]

After the large 24c8, the Eu(0)/Yb(0) nanoparticles were reacted with the much smaller 15c5, which, however, did not result in any suitable single crystal. Therefore, benzo-15-crown-5 (benzo-15c5) was used, as the π-stacking of aromatic systems often offers additional attractive interactions that may support crystallization. Indeed, the reaction of Eu(0)/Yb(0) nanoparticles with benzo-15c5 in [BMIm]I resulted in the compounds $[Eu(benzo\text{-}15c5)_2]I_2$ (**2**) (SI: Table S3 and Fig. S4) and $[Yb(benzo\text{-}15c5)_2]I_2$ (**3**) (SI: Table S4 and Fig. S5). Here, the $[BMIm]^+$ cation was reduced:[21,22]

$$M(0) + 2\ \text{benzo-15c5} + 2\ [BMIm]I \rightarrow [M(benzo\text{-}15c5)_2]I_2 + 2\ C_8H_{14}N_2 + H_2 \quad (M = Eu, Yb)$$

2 and **3** contain similar sandwich-type $[M(benzo\text{-}15c5)_2]^{2+}$ cations (Table 2 and Fig. 3b, c). The benzyl groups indeed show π-stacking (SI: Fig. S4 and S5). Eu^{2+} and Yb^{2+} are coordinated by all five oxygen atoms of both benzo-15c5 molecules, resulting in a pentagonal antiprismatic coordination (Eu–O: 269.2(4)–275.5(5) pm; Yb–O: 262.8(4)–271.5(5) pm; Table 2). Due to the larger size of Eu^{2+}, the Eu–O distances are, as expected, longer than the Yb–O distances.

In addition to benzo-15c5, the Eu(0) and Yb(0) nanoparticles were reacted with *N*-phenylaza-15-crown-5 (pac), showing a similar ring opening but with one oxygen atom replaced by nitrogen. Here, the compounds $[BMIm][Eu_4Cl_4(pac)_4][AlCl_4]_5$ (**4**) (SI: Table S5 and Fig. S6) and $[\{Yb(pac)\}_2(\mu\text{-}Cl)_2][AlCl_4]_2$ (**5**) (SI: Table S6 and Fig. S7) were obtained with formation of aluminum metal:

$$12\ Eu(0) + 12\ pac + 3\ [BMIm][AlCl_4] + 20\ AlCl_3 \rightarrow 3\ [BMIm][Eu_4Cl_4(pac)_4][AlCl_4]_5 + 8\ Al$$

$$6\ Yb(0) + 6\ pac + 10\ AlCl_3 \rightarrow 3\ [\{Yb(pac)\}_2(\mu\text{-}Cl)_2][AlCl_4]_2 + 4\ Al$$

Although the conditions of reaction were similar, interestingly, totally different compositions and structures were obtained for europium and ytterbium (Fig. 4a and b). Thus, **4**, as the central building unit, contains a distorted Eu_4Cl_4 heterocubane (Eu–Cl: 287(4)–316(3) pm; Cl–Eu–Cl: 71.6(8)–86.8(6)°; Table 2) with each Eu^{2+} additionally coordinated by a pac molecule *via* all four oxygen atoms (Eu–O: 247.0(16)–270.5(14) pm; Table 2) as well as the nitrogen atom (Eu–N: 223.9(18)–281.3(17) pm; Table 2). As a result, Eu^{2+} exhibits an eightfold coordination (Table 2). Although heterocubane-type building units are well-known, in principle, such an arrangement is unusual for europium, so that **4** contains the first Eu_4X_4 heterocubane (Fig. 4a). In contrast to **4**, **5** is a dinuclear complex with two Yb^{2+} atoms bridged by two chlorine atoms (Yb–Cl: 274.45(13)–277.19(13) pm; Table 2 and Fig. 4a). Furthermore, each Yb^{2+} is coordinated by all four oxygen atoms and the nitrogen atom of

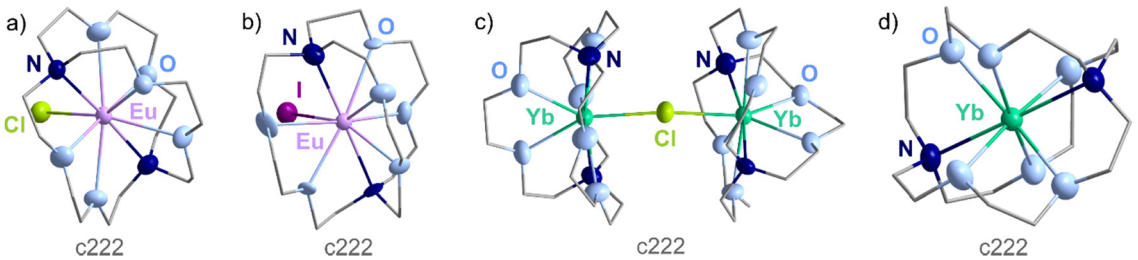

Fig. 5 Structure of (a) the $[EuCl(c222)]^+$ cation in **6**, (b) the $[EuI(c222)]^+$ cation in **7**, (c) the $[\{Yb(c222)\}_2(\mu\text{-}Cl)]^{3+}$ cation in **8**, (d) the $[Yb(c222)]^{2+}$ cation in **9** (unit cells displayed in SI: Fig. S8–S11).

Table 2 Selected structural details of the compounds **1–11** (Ln: Eu, Yb) with coordination of Eu^{2+}/Yb^{2+} and distances to ligands

Compound	Space group	Coordination	Distances/pm		
			Ln–O	Ln–N	Ln–X
$[Yb(24c8)]_4[AlCl_4]_8$·THF (**1**)	$P4_2/nmc$	8(O)	246(1)–248(1)	—	≥543(1)
$[Eu(benzo\text{-}15c5)_2]I_2$ (**2**)	$P2_1/c$	10(O)	269(1)–276(1)	—	≥557(1)
$[Yb(benzo\text{-}15c5)_2]I_2$ (**3**)	$P2_1/n$	10(O)	263(4)–272(1)	—	≥549(1)
$[BMIm][Eu_4Cl_4(pac)_4][AlCl_4]_5$ (**4**)	$P2_12_12_1$	4(O) + 1(N) + 3(Cl)	247(1)–271(1)	224(2)–281(2)	287(1)–316(1)
$[\{Yb(pac)\}_2(\mu\text{-}Cl)_2][AlCl_4]_2$ (**5**)	$P2_1/c$	4(O) + 1(N) + 2(Cl)	244(1)–252(1)	260(1), 264(1)	275(1), 277(1)
$[EuCl(c222)][AlCl_4]$ (**6**)	$P2_1$	6(O) + 2(N) + 1(Cl)	267(1)–276(1)	285(2), 288(1)	283(1)
[EuI(c222)]I (**7**)	$P42_12$	6(O) + 2(N) + 1(I)	258(1)–296(1)	266(1), 275(1)	335(1)
$[\{Yb(c222)\}_2(\mu\text{-}Cl)][AlCl_4]_6$·1.5THF (**8**)	Pc	6(O) + 2(N) + 1(Cl)	250(1)–271(1)	277(1)–283(1)	273(1), 274(1)
$[BMIm][Yb(c222)]I_3$ (**9**)	$P2_1/c$	6(O) + 2(N)	247(1)–249(1)	262(1), 263(1)	≥599(1)
$[Eu(k21)_2]I_2$·naph (**10**)	$P2_1/n$	6(O) + 4(N)	274(1)–284(1)	278(1)–286(1)	≥574(1)
$[BMIm][\{Yb(k21)\}_2(\mu\text{-}Cl)_3]I_2$ (**11**)	$C2/c$	3(O) + 2(N) + 3(Cl)	253(1)–262(1)	259(1)–262(1)	279(1), 295(1)

pac (Yb–O: 244.1(4)–252.4(3) pm; Yb–N: 260.0(4)–264.4(5) pm; Table 2). In accordance with its smaller size, Yb^{2+} in **5** shows sevenfold coordination, whereas the larger Eu^{2+} in **4** exhibits eightfold coordination.

Aiming at an even more rigid coordination, the Eu(0) and Yb(0) nanoparticles were next reacted with the cage-like [2.2.2]cryptand (c222). Here, a reaction of Eu(0) nanoparticles in [BMIm]Cl/$AlCl_3$ resulted in colorless crystals of $[EuCl(c222)][AlCl_4]$ (**6**), again with the reduction of aluminium (SI: Table S7 and Fig. S8):

$$3\ Eu(0) + 3\ c222 + 5\ AlCl_3 \rightarrow 3\ [EuCl(c222)][AlCl_4] + 2\ Al$$

In **6**, Eu^{2+} was successfully encapsulated by c222 and is coordinated by six oxygen atoms (Eu–O: 267.1(13)–276.3(7) pm) and two nitrogen atoms (Eu–N: 284.9(16)–287.9(15) pm) of c222 as well as by one Cl^- (Eu–Cl: 283.1(2) pm) (Table 2). The resulting ninefold coordination and coordinative arrangement is designated in the literature as the ''hula-hoop'' geometry (Fig. 5a).[25] A reaction of Eu(0) nanoparticles in [BMIm]I resulted in [EuI(c222)]I (**7**) with similar building units (SI: Table S8 and Fig. S9), however, with the reduction of $[BMIm]^+$:

$$Eu(0) + c222 + 2\ [BMIm]I \rightarrow [EuI(c222)]I + 2\ C_8H_{14}N_2 + H_2$$

Eu^{2+} is coordinated similar to **6** by six oxygen atoms (Eu–O: 260(4)–287(5) pm) and two nitrogen atoms (Eu–N: 236(4)–261(3) pm) of c222 and one I^- (Eu–I: 334.7(1) pm) (Table 2), again, with a ''hula-hoop'' geometry (Fig. 5b).

While the reaction of Eu(0) nanoparticles with c222 in [BMIm][$AlCl_4$] and [BMIm]I led to similar compounds, the reaction of Yb(0) nanoparticles with c222 resulted in different products. In this regard, colorless crystals of $[\{Yb(c222)\}_2(\mu\text{-}Cl)]_2[AlCl_4]_6$·1.5THF (**8**) were obtained in [BMIm][$AlCl_4$] (SI: Table S9 and Fig. S10), whereas $[BMIm][Yb(c222)]I_3$ (**9**) was obtained in [BMIm]I (SI: Table S10 and Fig. S11) with either the reduction of aluminium or $[BMIm]^+$:

$$12\ Yb(0) + 12\ c222 + 26\ AlCl_3 + 4.5THF \rightarrow 3\ [\{Yb(c222)\}_2(\mu\text{-}Cl)]_2[AlCl_4]_6\cdot 1.5THF + 8\ Al$$

$$Yb(0) + c222 + 3\ [BMIm]I \rightarrow [BMIm][Yb(c222)]I_3 + 2\ C_8H_{14}N_2 + H_2$$

8 is a dinuclear complex with two Yb^{2+} bridged by one Cl^- (Fig. 5c). In addition to chlorine (Yb–Cl: 272.7(4)–274.1(4) pm), Yb^{2+} is coordinated by all oxygen atoms (Yb–O: 250.3(10)–271.2(11) pm) and two nitrogen atoms (Yb–N: 277.3(11)–282.7(14) pm) of c222 (Table 2). Similar to **6** and **7**, **8** also shows a ''hula-hoop'' geometry and represents the first example of such a dinuclear Yb^{2+} complex. Until now only a mononuclear cation $[YbI(c222)_2]^+$ was described, which shows comparable distances (Yb–N: 279 pm; Yb–O: 248–256 pm; and Yb–I: 329.1 pm).[26] The elongated Yb–O distances in **8** can be attributed to the bridged, dinuclear structure and the steric demand of two c222 molecules. Finally, a non-coordinated molecule of THF in the unit cell of **8** should be noticed, which – similar to **1** – originates from the synthesis of Yb(0) nanoparticles and which is not coordinated to the cation. The coordinative situation of **9** is significantly different from **8** with Yb^{2+} coordinated like a distorted cube with six oxygen atoms (Yb–O: 247.3(5)–249.4(5) pm) and two nitrogen atoms (Yb–N: 261.7(6)–262.8(6) pm) of c222 (Table 2 and Fig. 5d) but without a coordination of Yb^{2+} to the halide. Instead, three I^- anions and a $[BMIm]^+$ cation are located between the $[Yb(c222)]^{2+}$ cations with long distances (Yb–I: 599(1) pm; Table 2). A $[Yb(c222)]^{2+}$ cation was also reported before in $[Yb(c222)][Yb(CpSiMe_3)_3]_2$ and exhibits similar distances as in **9** (Yb–O: 244.4–253.9 pm; Yb–N: 261.3–263.4 pm).[27]

Finally, kryptofix21 (k21) was examined as an N–H acidic cyclic ether to react with Eu(0) and Yb(0) nanoparticles. In addition to the oxidation of Eu(0)/Yb(0) by reduction of Al^{3+} or reduction of $[BMIm]^+$, k21 itself may serve as an oxidizing agent with the formation of H_2 and the anions $[k21]^-$ or $[k21]^{2-}$. Such behaviour of N–H acidic aza-crown ethers is well-known in the literature.[28] Eu(0) nanoparticles and k21 nevertheless show the reduction of $[BMIm]^+$ in [BMIm]I without any deprotonation of k21 and with the formation of colourless crystals of $[Eu(k21)_2]I_2$·naph (**10**) (SI: Table S11 and Fig. S12):

$$Eu(0) + 2\ k21 + 2\ [BMIm]I + naph \rightarrow [Eu(k21)_2]I_2\cdot naph + 2\ C_8H_{14}N_2 + H_2$$

For the first time, we here observe the incorporation of naphthalene, which – similar to THF in **1** and **8** – originates from the synthesis of Eu(0) nanoparticles and which is – similar to THF – not coordinated to the cation.

10 exhibits a sandwich-type $[Eu(k21)_2]^{2+}$ cation (Fig. 4c). Eu^{2+} is coordinated by three oxygen atoms (Eu–O: 273.7(4)–283.8(4) pm) and two nitrogen atoms (Eu–N: 277.9(4)–286.0(4) pm) of both k21 molecules (Table 2), resulting in a ten-fold, pentagonal antiprismatic coordination. The C–N–C angles at the nitrogen atoms of k21, moreover, indicate a distorted tetrahedral arrangement (113.2(5)–117.8(5)°), which points to the presence of the H atom. Moreover, two I^- ions serve as anions in **10** with long Eu–I distances (574(1) pm; SI: Fig. S12).

The reaction of Yb(0) nanoparticles with k21 in [BMIm]I is different from the aforementioned Eu(0) nanoparticles and resulted in the dinuclear complex $[BMIm][\{Yb(k21)\}_2(\mu\text{-}Cl)_3]I_2$ (**11**) (SI: Table S12 and Fig. S13). Again, $[BMIm]^+$ is preferred as an oxidizing agent over k21:

$$2\ Yb(0) + 2\ k21 + 3\ LiCl + 5\ [BMIm]I \rightarrow [BMIm][\{Yb(k21)\}_2(\mu\text{-}Cl)_3]I_2 + 4\ C_8H_{14}N_2 + 2\ H_2 + 3\ LiI$$

Besides I^- from the ionic liquid, it must be noticed that Cl^- is also involved in the composition of **11**. Its presence can be related to the formation of LiCl in the synthesis of the Yb(0) nanoparticles. As only small amounts of LiCl may remain after the purification of the Yb(0) nanoparticles, only low amounts of **11** were obtained (about 20% yield), which is much below the yield of other compounds (*e.g.* **1–6** with quantitative yields related to the amount of the cyclic ether). Yb^{2+} in **11** is coordinated by three oxygen atoms (Yb–O: 252.7(6)–261.7(7) pm), both nitrogen atoms (Yb–N: 258.5(7)–261.7(8) pm) of k21 as well as by three bridging chlorine atoms (Yb–Cl: 278.7(2)–295.2(3) pm) (Table 2 and Fig. 4d). In summary, this results in a distorted, double-capped trigonal prism around Yb^{2+}. Such a triple chloride-bridged ytterbium dimer is already known[19,29] but here shown with a crown-ether ligand for the first time. The C–N–C angles of the nitrogen atoms of k21 again point to a tetrahedral arrangement (107.9(5)–115.5(8)°) and, thus, the presence of H atoms. Moreover, the presence of Cl^- and I^- as anions excludes k21 from being anionic as well.

In addition to single-crystal structure analysis, compounds **1–11** were examined by Fourier-transform infrared (FT-IR) spectroscopy (SI: Fig. S14). The spectra are dominated by the characteristic vibrations of the respective cyclic ethers (ν(C–H): 3100–2800 cm^{-1}; fingerprint area: 1500–750 cm^{-1}), which are shown as references as well. Moreover, $[BMIm]^+$ in **4**, **9**, and **11** (ν(C–H): 3000–2800 cm^{-1}; ν(C–N): 1200–1150 cm^{-1}) and $[AlCl_4]^-$ in **1**, **4–6**, and **8** (ν(Al–Cl): 550–450 cm^{-1}) are clearly visible. For **10**, the presence of naph is indicated by the characteristic vibration at 490 cm^{-1}. THF in **1** is indicated by its characteristic vibrations (ν(C–O) at 1100 and 900 cm^{-1}). Spectra of **10** and **11** clearly show N–H vibrations (ν(N–H): 3250–3150 cm^{-1}), which again exclude the deprotonation of k21. Finally, the absence of OH-related absorptions in the 3500–3000 cm^{-1} range proves the absence of moisture (SI: Fig. S14).

In summary, the novel redox approach using Eu(0)/Yb(0) nanoparticles as starting materials allows obtaining a variety of new compounds with Eu^{2+} and Yb^{2+} coordinated by 24c8, benzo-15c5, c222, pac, and k21 with different coordination scenarios, including mono-, di- and trinuclear complexes. The coordination clearly reflects the different radii of Eu^{2+} (139 pm, CN = 8) and Yb^{2+} (113 pm, CN = 8) as the largest and smallest divalent lanthanide ions.[5] Divalent lanthanides were occurring throughout. Besides the oxidation of the Eu(0)/Yb(0) nanoparticles, the redox approach resulted in the reduction of $[AlCl_4]^-$ to metallic aluminum if the ionic liquid contained Al^{3+} (*i.e.* $[BMIm][AlCl_4]$). If the ionic liquid does not contain Al^{3+} (*i.e.* [BMIm]I), $[BMIm]^+$ was reduced. The formation of hydrogen, as the third option in the case of k21, was not observed. Interestingly, compounds **1–11** only in few cases show the presence of THF (*i.e.* **1** and **8**) or naphthalene (*i.e.* **10**), although certain amounts of THF and/or naphthalene remain adsorbed on the surface of the Eu(0)/Yb(0) nanoparticles. In all these cases, THF and naphthalene are not coordinating the metal cation and, thus, do not disturb the chemistry and coordination of lanthanide-metal complexes.

Table 3 Excitation and emission of cyclic-ether compounds **1–11** with the maximum wavelength (λ_{max}) of excitation/emission and the full-width at half maximum (FWHM) of the emission (spectra of all compounds are shown in the SI, Fig. S15)

Compound	Excitation λ_{max}/nm	Emission λ_{max}/nm	Emission FWHM/nm
$[Yb(24c8)]_4[AlCl_4]_8$·THF (**1**)	398	470	131
$[Eu(benzo\text{-}15c5)_2]I_2$ (**2**)	369	419	82
$[Yb(benzo\text{-}15c5)_2]I_2$ (**3**)	395	467	124
$[BMIm][Eu_4Cl_4(pac)_4][AlCl_4]_5$ (**4**)	396	434	25
$[\{Yb(pac)\}_2(\mu\text{-}Cl)_2][AlCl_4]_2$ (**5**)	370	443	176
$[EuCl(c222)][AlCl_4]$ (**6**)	380	444	59
[EuI(c222)]I (**7**)	381	444	134
$[\{Yb(c222)\}_2(\mu\text{-}Cl)]_2[AlCl_4]_6$·1.5THF (**8**)	370	436	78
$[BMIm][Yb(c222)]I_3$ (**9**)	322	380	Weak emission
$[Eu(k21)_2]I_2$·naph (**10**)	396	468	149
$[BMIm][\{Yb(k21)\}_2(\mu\text{-}Cl)_3]I_2$ (**11**)	385	435	Weak emission

3.3 Optical properties

Since Eu^{2+} and Yb^{2+} are well-known luminescent centers, luminescence can be expected for all title compounds. Specifically, $4f^7 \rightarrow 4f^6 5d^1$ transitions may occur on Eu^{2+} and $4f^{14} \rightarrow 4f^{13}5d^1$ transitions on Yb^{2+}.[30] Since the d orbitals show strong coupling with the environment, the wavelength of excitation and emission depends on the respective coordination and compound. Indeed, all title compounds show emission at room temperature. Excitation and emission spectra exhibit the characteristic $4f^7 \rightarrow f^6 5d^1$ and $4f^{14} \rightarrow 4f^{13}5d^1$ transitions of Eu^{2+} and Yb^{2+} (Table 3, Fig. 6 and SI: Fig. S15). Excitation occurs in the UV to blue spectral regime with two absorption bands due to the splitting of the electronically excited state.[26,31] Emission is observed in the violet to blue spectral regime. For Yb^{2+}-containing compounds, the emission is generally weak, whereas the Eu^{2+}-containing compounds show good emission. As representative and most interesting compounds, the luminescence properties of $[Yb(24c8)]_4[AlCl_4]_8$·THF (**1**), $[BMIm][Eu_4Cl_4(pac)_4][AlCl_4]_5$ (**4**), $[EuCl(c222)][AlCl_4]$ (**6**), and

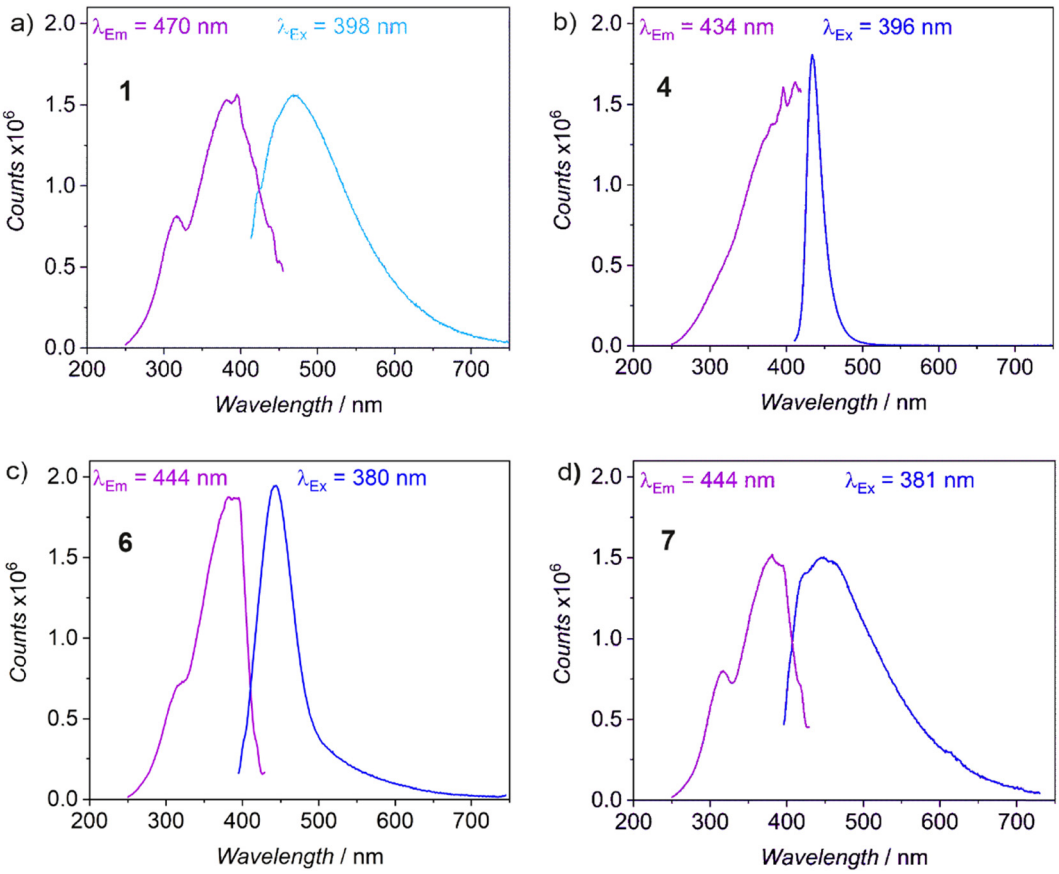

Fig. 6 Exemplary excitation and emission spectra of (a) $[Yb(24c8)]_4[AlCl_4]_8$·THF (**1**), (b) $[BMIm][Eu_4Cl_4(pac)_4][AlCl_4]_5$ (**4**), (c) [EuCl(c222)][$AlCl_4$] (**6**), and (d) [EuI(c222)]I (**7**) (spectra of all compounds shown in SI: Fig. S15).

[EuI(c222)]I (7) are displayed in Fig. 6 (SI: Fig. S15 with excitation/emission spectra of all compounds). $[Yb(24c8)]_4[AlCl_4]_8$·THF (**1**) shows typical emission of Yb^{2+}, which is comparably broad and low in intensity (Fig. 6a). Similarly, [EuI(c222)]I (7) is a typical representative for Eu^{2+}-based emission (Fig. 6d). The optical properties are comparable to known compounds such as [YbI(c222)]I, [EuBr(c222)]Br or $[EuI_2(c222)]$.[26,28a] In contrast, $[BMIm][Eu_4Cl_4(pac)_4][AlCl_4]_5$ (**4**) and [EuCl(c222)][$AlCl_4$] (**6**) exhibit a surprisingly narrow emission (Fig. 6b and c), which was rarely observed for Eu^{2+}. Specifically, **4** exhibits a very narrow emission band (FWHM of **4** with 25 nm *versus* 60–150 nm for **2**, **6**, **7**, and **10**; Table 3), which can be ascribed to the rigid coordination in the Eu_4Cl_4 heterocubane as indicated by the lowest coordination number (*i.e.* 8 for **4** *versus* 9 or 10 for **2**, **6**, **7**, and **10**) as well as the shortest Eu–O, Eu–N, and Eu–Cl distances (in comparison to **2**, **6**, **7**, and **10**). Moreover, the emission occurs at low wavelength in the blue spectral regime (<500 nm, Fig. 6b). In principle, such narrow-band blue-emitting features can be interesting for organic light-emitting diodes (OLEDs) to replace the current Ru- or Ir-containing dyes.[32] By comparison with the naked eye, **6** shows the most intense emission. Here, a quantum yield of 54(2)% was determined, which, however, could be lowered (by about 3–5%) due to ionic liquid remaining adsorbed on the surface of microcrystals of **6**.[7b]

The compounds **4**, **6**, **7**, and **9** crystallize in space groups without inversion symmetry, so that, besides luminescence, non-linear optical (NLO) effects can also be expected. As **6** already showed good luminescence properties and as the compound can be prepared with high yield and purity (see the SI), this compound with the space group $P2_1$ was also evaluated with regard to NLO effects with the example of second harmonic generation (SHG). To this concern, the Kurtz–Perry approach was applied,[33] which offers several advantages for the characterization of newly discovered compounds. First of all, SHG measurements can be performed with microcrystalline powder samples. Moreover, the presence of enantiomeric or twinned crystals is not an issue if the individual domains are large enough (>1 μm). The Kurtz–Perry approach also has some limitations. Thus, it only provides information about the averaged effective SHG coefficient with a large uncertainty because it is often difficult to quantify the grain-size distribution in powder samples. According to light microscopy, the grain size of powder samples of **6** was estimated to 5–50 μm.

Two different laser sources were used as the fundamental pump wave. The first laser source has a single wavelength of 1064 nm. Table 4 shows the results of the conversion from 1064 nm to SHG intensities at 532 nm. The crystals are colorless, so that **6** is transparent in the spectral range of the

Table 4 SHG intensities of [EuCl(c222)][$AlCl_4$] (**6**) at 532 nm and of selected references

Sample	Particle size/μm	SHG intensity/mV
Quartz	<5	29(10)
Quartz	5–25	238(38)
Quartz	25–50	380(81)
Al_2O_3	9	0(1)
KDP	5–25	730(38)
KDP	25–50	1932(367)
[EuCl(c222)][$AlCl_4$] (**6**)	5–50	1723(421)

incident laser light as well as in the spectral range of the converted light. As the Kurtz–Perry approach does not result in absolute SHG intensities, quartz and potassium dihydrogenphosphate (KH_2PO_4, KDP) were examined as references under similar conditions to **6** to assess the strength of the SHG signal. KDP is phase matchable (second-order susceptibility: d_{36} = 0.39 pm V^{-1}), and therefore yields a SHG signal that is at least 5 times stronger than for the nonphase-matchable quartz (d_{11} = 0.3 pm V^{-1})[34] although the SHG coefficients of both reference samples are similar. Corundum (α-Al_2O_3) was analyzed as an additional reference showing inversion symmetry and, therefore, no SHG effect at all. Based on this comparison, a strong SHG signal was determined for **6**, which is comparable to KDP (Table 4). Additional measurements of the grain-size dependence of the SHG signals could provide further experimental constraints for the phase-matching conditions but were outside the scope of the present study.

The second pump source is a broadband laser with a wavelength of 950–1300 nm. Fig. 7 shows the conversion of such a broadband laser for sample **6** and the references. The considerably strong SHG signals of **6** confirm the non-centrosymmetric structure of [EuCl(c222)][$AlCl_4$]. The intensity distribution of the pump laser dominates the wavelength-dependent shape of the SHG signal, especially in the 520–650 nm range.

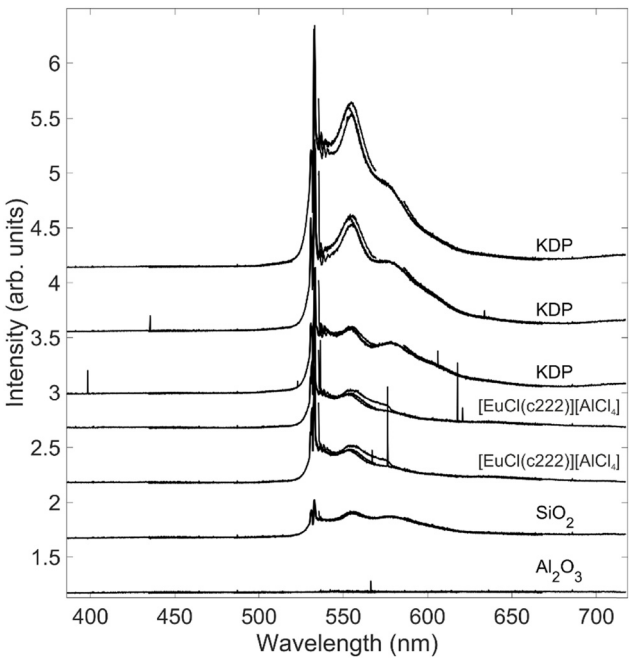

Fig. 7 Second harmonic generation (SHG) spectra of [EuCl(c222)][$AlCl_4$] (**6**) with KDP, SiO_2 and Al_2O_3 as references using a broadband laser as a pump source ranging from 950 to 1300 nm.

4. Conclusions

The novel cyclic-ether complexes [Yb(24c8)]$_4$[$AlCl_4$]$_8$·THF (**1**), [Eu(benzo-15c5)$_2$]I_2 (**2**), [Yb(benzo-15c5)$_2$]I_2 (**3**), [BMIm][Eu_4Cl_4-(pac)$_4$][$AlCl_4$]$_5$ (**4**), [{Yb(pac)}$_2$(μ-Cl)$_2$][$AlCl_4$]$_2$ (**5**), [EuCl(c222)]-[$AlCl_4$] (**6**), [EuI(c222)]I (**7**), [{Yb(c222)}$_2$(μ-Cl)]$_2$[$AlCl_4$]$_6$·1.5THF (**8**), [BMIm][Yb(c222)]I_3 (**9**), [Eu(k21)$_2$]I_2·naph (**10**), and [BMIm][{Yb(k21)}$_2$(μ-Cl)$_3$]I_2 (**11**) were prepared *via* a redox approach, using europium and ytterbium metal nanoparticles as starting materials. The Eu(0) and Yb(0) nanoparticles were synthesized in the liquid phase by reduction of EuI_2 and $YbCl_3$ with lithium naphthalenide in THF. They are monocrystalline and exhibit a size of 3.8 ± 0.8 nm (Eu(0)) and 2.0 ± 0.3 nm (Yb(0)).

Eu(0) and Yb(0) nanoparticles were selected as both are flexible in terms of their oxidation state (II/III), and cover the range of possible radii from $r(Eu^{2+})$: 139 pm to $r(Yb^{3+})$: 113 pm in the 4f row (all radii for coordination number 8). They were made to react with the cyclic ethers 24-crown-8/24c8, benzo-15-crown-5/benzo-15c5, *N*-phenylaza-15-crown-5/pac, [2.2.2]cryptand/c222, and kryptofix21/k21 to probe the formation of lanthanide-metal complexes, specifically with usually less preferred ligands such as 15c5 and 24c8 being too small or too large with regard to the size of the lanthanide cation as well as the sterically more demanding cryptand or the nitrogen-containing aza-crown ethers. **1–11** show very different structural and coordinative scenarios, mono- to tetranuclear building units as well as interesting structural and optical properties with luminescence and strong, KDP-comparable second-harmonic generation. Specifically interesting are the 24c8-coordination of Yb^{2+} in **1**, the tetranuclear [$Eu_4Cl_4(pac)_4$]$^{4+}$ cation in **4**, the ''hula-hoop''-like arrangements in **6**, **7**, and **8**, the single-, double- and triple-bridging *via* chlorine in **8**, **5** and **11**, respectively, as well as the narrow-line blue emission of **4** and the strong KDP-like SHG effect of **6**. Generally, the redox approach used here with suspended reactive metal nanoparticles could be an interesting addition to the synthesis tools of novel metal complexes with cyclic ethers and promising structural, optical, magnetic or catalytic properties, specifically, if the size, coordination, and/or binding of the respective metal cation and cyclic ether are non-optimal.

Conflicts of interest

The authors declare no competing financial interest.

Data availability

Additional data regarding experiments and methods can be obtained from the supplementary information (SI) and from the authors upon request. Supplementary information: details

regarding analytical techniques, synthesis of the title compounds, crystallographic details and spectroscopic and thermal analysis. See DOI: https://doi.org/10.1039/d5tc02776d.

CCDC 2443450 (**1**), 2443451 (**2**), 2443452 (**3**), 2443453 (**4**), 2443454 (**5**), 2443455 (**6**), 2443456 (**7**), 2443457 (**8**), 2443458 (**9**), 2443459 (**10**) and 2443460 (**11**) contain the supplementary crystallographic data for this paper.[35a–k]

Acknowledgements

The authors acknowledge the Deutsche Forschungsgemeinschaft (DFG) for funding within the Collaborative Research Center 1573 ''4f for Future'' (project A4). We acknowledge the Karlsruhe Nano Micro Facility (KNMF), especially Prof. Dr D. Fenske, for data collection of compounds **8**, **9** and **11** using a Stoe StadiVari diffractometer with a Ga-metal-jet source. Additionally, we thank Dr M. T. Gamer and Prof. Dr P. W. Roesky for data collection of compound **4** using a Stoe Stadivari diffractometer with a Mo-microfocus source.

References

1 Z. Liu, S. K. M. Nalluri and J. F. Stoddart, *Chem. Soc. Rev.*, 2017, **46**, 2459–2478.
2 J. Li, D. Yim, W.-D. Jang and J. Yoon, *Chem. Soc. Rev.*, 2017, **46**, 2437–2458.
3 W.-L. Zhou, Y. Chen, W. Lin and Y. Liu, *Chem. Commun.*, 2021, **57**, 11443–11456.
4 (*a*) K. Atal, U. Phageria, S. Kumari, Y. Dhayal and S. Bugalia, *Inorg. Chim. Acta*, 2024, **561**, 121857; (*b*) D. N. Kulasekara, A. B. Kajjam, S. Praneeth, T. M. Dittrich and M. J. Allen, *ACS Appl. Mater. Interfaces*, 2023, **15**, 42037–42045; (*c*) Y. Liu, B.-H. Han and Y.-T. Chen, *Coord. Chem. Rev.*, 2000, **200–202**, 53–73; (*d*) N.-D. H. Gamage, Y. Mei, J. Garcia and M. J. Allen, *Angew. Chem., Int. Ed.*, 2010, **49**, 8923–8925.
5 R. D. Shannon, *Acta Crystallogr., Sect. A*, 1976, **32**, 751–767.
6 J. S. Bradshaw, R. M. A. Izatt, V. Bordunov, C. Y. Zhu and J. K. Hathaway, Crown ethers, in *Comprehensive Supramolecular Chemistry*, ed. G. W. Gokel, 1996, vol. 1, p. 35.
7 (*a*) N. Hamon, L. Godec, S. Sanchez, M. Beyler, L. J. Charbonniere and R. Tripier, *Angew. Chem., Int. Ed.*, 2025, **64**, e202414608; (*b*) T. N. Poe, A. N. Gaiser and T. E. Albrecht-Schonzart, *Cryst. Growth Des.*, 2022, **22**, 2670–2678; (*c*) A. Topor, D. Avram, R. Dascalu, C. Maxim, C. Tiseanu and M. Andruh, *Dalton Trans.*, 2021, **50**, 9881–9890; (*d*) E. Merzlyakova, S. Wolf, S. Lebedkin, L. Bayarjargal, B. L. Neumeier, D. Bartenbach, C. Holzer, W. Klopper, B. Winkler, M. Kappes and C. Feldmann, *J. Am. Chem. Soc.*, 2021, **143**, 798–804; (*e*) M. Al Hareri, Z. Ras Ali, J. Regier, E. L. Gavey, L. D. Carlos, R. A. S. Ferreira and M. Pilkington, *Inorg. Chem.*, 2017, **56**, 7344–7353; (*f*) S. Petrosyants, Z. Dobrokhotova, A. Ilyukhin, N. Efimov, Y. Mikhlina and V. Novotortsev, *Inorg. Chim. Acta*, 2015, **434**, 41–50.
8 (*a*) W.-J. Xu, Q.-C. Luo, Z.-H. Li, Y.-Q. Zhai and Y.-Z. Zheng, *Adv. Sci.*, 2024, **11**, 2308548; (*b*) A. Borah, S. Dey, S. K. Gupta, G. Rajaraman and R. Murugavel, *Dalton Trans.*, 2023, **52**, 8943–8955; (*c*) Y. Gil, L. Llanos, P. Cancino, P. Fuentealba, A. Vega, E. Spodine and D. Aravena, *J. Phys. Chem. C*, 2020, **124**, 5308–5320; (*d*) M. Xemard, M. Cordier, F. Molton, C. Duboc, B. Le Guennic, O. Maury, O. Cador and G. Nocton, *Inorg. Chem.*, 2019, **58**, 2872–2880; (*e*) L. Maxwell, M. Amoza and E. Ruiz, *Inorg. Chem.*, 2018, **57**, 13225–13234; (*f*) F. Gao, F.-L. Yang, X. Feng, H. Xu, W. Sun, H. Liu and X.-L. Li, *Dalton Trans.*, 2017, **46**, 1317–1323; (*g*) H. Wada, S. Ooka, T. Yamamura and T. Kajiwara, *Inorg. Chem.*, 2017, **56**, 147–155.
9 (*a*) H. Nagae, R. Aoki, S.-N. Akutagawa, J. Kleemann, R. Tagawa, T. Schindler, G. Choi, T. P. Spaniol, H. Tsurugi and J. Okuda, *et al.*, *Angew. Chem., Int. Ed.*, 2018, **57**, 2492–2496; (*b*) Z.-M. Zhang, S. Yao, Y.-G. Li, X.-B. Han, Z.-M. Su, Z.-S. Wang and E.-B. Wang, *Chem. – Eur. J.*, 2012, **18**, 9184–9188; (*c*) T. Hamada, K. Manabe, S. Ishikawa, S. Nagayama, M. Shiro and S. Kobayashi, *J. Am. Chem. Soc.*, 2003, **125**, 2989–2996.
10 The American Chemical Society (ACS), Program package Scifinder, Washington, 2025.
11 (*a*) M. L. Marsh, F. D. White, D. S. Meeker, C. D. McKinley, D. Dan, C. Van Alstine, T. N. Poe, D. L. Gray, D. E. Hobart and T. E. Albrecht-Schmitt, *Inorg. Chem.*, 2019, **58**, 9602–9612; (*b*) J. L. Atwood, L. J. Barbour, S. Dalgarno, C. L. Raston and H. R. Webb, *J. Chem. Soc., Dalton Trans.*, 2002, 4351–4356; (*c*) C. Platas, F. Avecilla, A. de Blas, C. F. G. C. Geraldes, T. Rodriguez-Blas, H. Adams and J. Mahia, *Inorg. Chem.*, 1999, **38**, 3190–3199.
12 (*a*) L. Maria, I. C. Santos, L. G. Alves, J. Marcalo and A. M. Martins, *J. Organomet. Chem.*, 2013, **728**, 57–67; (*b*) M. Gonzalez-Lorenzo, C. Platas-Iglesias, M. Mato-Iglesias, D. Esteban-Gomez, A. de Blas and T. Rodriguez-Blas, *Polyhedron*, 2008, **27**, 1415–1422; (*c*) S. Dalgarno and C. L. Raston, *Dalton Trans.*, 2003, 287–290.
13 (*a*) D. Bartenbach, O. Wenzel, R. Popescu, L. Faden, A. Reiß, M. Kaiser, A. Zimina, J. Grunwaldt, D. Gerthsen and C. Feldmann, *Angew. Chem., Int. Ed.*, 2021, **60**, 17373–17377; (*b*) C. Schöttle, P. Bockstaller, R. Popescu, D. Gerthsen and C. Feldmann, *Angew. Chem., Int. Ed.*, 2015, **54**, 9866–9870.
14 P. Calandra, D. Lombardo, F. Neri, A. Ruggirello, S. Trusso and V. T. Liveri, *Mater. Lett.*, 2010, **64**, 576–579.
15 J. A. Ascencio, A. C. Rodríguez-Monroy, H. B. Liu and G. Canizal, *Chem. Lett.*, 2004, **33**, 1056–1057.
16 N. Wiberg, E. Wiberg and A. F. Holleman, *Anorganische Chemie*, de Gruyter, Berlin, 103rd edn, 2017, vol. 1, Annex III/IV.
17 K. Takemur and K. Syassen, *J. Phys. F*, 1985, **15**, 543–559.
18 B. J. Beaudry and P. E. Palmer, *J. Less-Common Met.*, 1974, **34**, 225–231.
19 Y. Yao, Y. Zhang, Q. Shen and K. Yu, *Organometallics*, 2002, **21**, 819–824.
20 J. Wu, P. Xie, W. Hao, D. Lu, Y. Qi and Y. Mi, *Front. Chem.*, 2022, **10**, 1014893.
21 (*a*) S. Wellens, N. R. Brooks, B. Thijs, L. Van Meervelt and K. Binnemans, *Dalton Trans.*, 2014, **43**, 3443–3452; (*b*) F. E. Hahn

and M. C. Jahnke, *Angew. Chem., Int. Ed.*, 2008, **47**, 3122–3172; (*c*) M. C. Kroon, W. Buijs, C. J. Peters and G. J. Witkamp, *Green Chem.*, 2006, **8**, 241–245.

22 (*a*) J. Feng, S. Zeng, H. Liu, J. Feng, H. Gao, L. Bai, H. Dong, S. Zhang and X. Zhang, *ChemSusChem*, 2018, **11**, 3191–3197; (*b*) L. E. Barrosse-Antle and R. G. Compton, *Chem. Commun.*, 2009, 3744–3746; (*c*) B. Gorodetsky, T. Ramnial, N. R. Branda and J. A. C. Clyburne, *Chem. Commun.*, 2004, 1972–1973.

23 (*a*) L. Faden, A. Reiß, R. Popescu, C. Donsbach, J. Göttlicher, T. Vitova, D. Gerthsen and C. Feldmann, *Inorg. Chem.*, 2024, **63**, 1020–1034; (*b*) M. Liebertseder, C. Donsbach and C. Feldmann, *RSC Adv.*, 2023, **13**, 11441–11449.

24 M. A. Bonnin, S. Leicht and C. Feldmann, *Inorg. Chem.*, 2025, **64**, 723–730.

25 C. U. Lenora, F. Carniato, Y. Shen, Z. Latif, E. M. Haacke, P. D. Martin, M. Botta and M. J. Allen, *Chem. – Eur. J.*, 2017, **23**, 15404–15414.

26 T. C. Jenks, A. N. W. Kuda-Wedagedara, M. D. Bailey, C. L. Ward and M. J. Allen, *Inorg. Chem.*, 2020, **59**, 2613–2620.

27 D. N. Huh, C. M. Kotyk, M. Gembicky, A. L. Rheingold, J. W. Ziller and W. J. Evans, *Chem. Commun.*, 2017, **53**, 8664–8666.

28 (*a*) W. Yan, T. Li, Z. Cai, H. Qi, R. Guo, P. Huo, Z. Liu and Z. Bian, *Inorg. Chem. Front.*, 2022, **9**, 4794–4800; (*b*) F. Benetollo, G. Bombieri, G. Depaoli and M. R. Truter, *Inorg. Chim. Acta*, 1996, **245**, 223–229.

29 Z. Q. Zhang, Y. M. Yao, Y. Zhang, Q. Shen and W. T. Wong, *Inorg. Chim. Acta*, 2004, **357**, 3173–3180.

30 (*a*) W. Li, H. Fujikawa, G. Y. Adachi and J. Shiokawa, *Inorg. Chim. Acta*, 1986, **117**, 87–89; (*b*) H. Terraschke and C. Wickleder, *Chem. Rev.*, 2015, **115**, 11352–11378.

31 J. Jiang, N. Higashiyama, K. I. Machida and G. Y. Adachi, *Coord. Chem. Rev.*, 1998, **170**, 1–29.

32 J.-H. Lee, C.-H. Chen, P.-H. Lee, H.-Y. Lin, M. Leung, T.-L. Chiu and C.-F. Lin, *J. Mater. Chem. C*, 2019, **7**, 5874–5888.

33 S. K. Kurtz and T. T. Perry, *J. Appl. Phys.*, 1968, **39**, 3789–3818.

34 L. Garvie, P. Rez, J. Alvarez, P. Buseck, A. Craven and R. Brydson, *Am. Mineral.*, 2000, **85**, 732–738.

35 (*a*) CCDC 2443450: Experimental Crystal Structure Determination, 2025, DOI: **10.5517/ccdc.csd.cc2n0lz8**; (*b*) CCDC 2443451: Experimental Crystal Structure Determination, 2025, DOI: **10.5517/ccdc.csd.cc2n0m0b**; (*c*) CCDC 2443452: Experimental Crystal Structure Determination, 2025, DOI: **10.5517/ccdc.csd.cc2n0m1c**; (*d*) CCDC 2443453: Experimental Crystal Structure Determination, 2025, DOI: **10.5517/ccdc.csd.cc2n0m2d**; (*e*) CCDC 2443454: Experimental Crystal Structure Determination, 2025, DOI: **10.5517/ccdc.csd.cc2n0m3f**; (*f*) CCDC 2443455: Experimental Crystal Structure Determination, 2025, DOI: **10.5517/ccdc.csd.cc2n0m4g**; (*g*) CCDC 2443456: Experimental Crystal Structure Determination, 2025, DOI: **10.5517/ccdc.csd.cc2n0m5h**; (*h*) CCDC 2443457: Experimental Crystal Structure Determination, 2025, DOI: **10.5517/ccdc.csd.cc2n0m6j**; (*i*) CCDC 2443458: Experimental Crystal Structure Determination, 2025, DOI: **10.5517/ccdc.csd.cc2n0m7k**; (*j*) CCDC 2443459: Experimental Crystal Structure Determination, 2025, DOI: **10.5517/ccdc.csd.cc2n0m8l**; (*k*) CCDC 2443460: Experimental Crystal Structure Determination, 2025, DOI: **10.5517/ccdc.csd.cc2n0m9m**.